Photoacoustics 5 (2017) 25–35

Contents lists available at ScienceDirect

Photoacoustics

journal homepage: www.elsevier.com/locate/pacs

Research article

Photoacoustic signal characterization of cancer treatment response: Correlation with changes in tumor oxygenation

Eno Hysi[a,b], Lauren A. Wirtzfeld[a,b], Jonathan P. May[c], Elijus Undzys[d], Shyh-Dar Li[c], Michael C. Kolios[a,b,*]

[a] Department of Physics, Ryerson University, Toronto, M5 B 2K3, Canada
[b] Institute for Biomedical Engineering, Science and Technology, Li Ka Shing Knowledge Institute, Keenan Research Center, St. Michael's Hospital, Toronto, M5 B 1T8, Canada
[c] Faculty of Pharmaceutical Sciences, The University of British Colombia, Vancouver, V6T 1Z3, Canada
[d] Drug Delivery and Formulation Group, Ontario Institute for Cancer Research, Toronto, M5G 0A3, Canada

ARTICLE INFO

Article history:
Received 13 August 2016
Received in revised form 18 January 2017
Accepted 13 March 2017
Available online 21 March 2017

Keywords:
Photoacoustic and ultrasound tissue characterization
Cancer treatment monitoring
Radiofrequency analysis
Oxygen saturation
Tumor blood vessels

ABSTRACT

Frequency analysis of the photoacoustic radiofrequency signals and oxygen saturation estimates were used to monitor the in-vivo response of a novel, thermosensitive liposome treatment. The liposome encapsulated doxorubicin (HaT-DOX) releasing it rapidly (<20 s) when the tumor was exposed to mild hyperthermia (43 °C). Photoacoustic imaging (VevoLAZR, 750/850 nm, 40 MHz) of EMT-6 breast cancer tumors was performed 30 min pre- and post-treatment and up to 7 days post-treatment (at 2/5/24 h timepoints). HaT-DOX-treatment responders exhibited on average a 22% drop in oxygen saturation 2 h post-treatment and a decrease (45% at 750 nm and 73% at 850 nm) in the slope of the normalized PA frequency spectra. The spectral slope parameter correlated with treatment-induced hemorrhaging which increased the optical absorber effective size via interstitial red blood cell leakage. Combining frequency analysis and oxygen saturation estimates differentiated treatment responders from non-responders/control animals by probing the treatment-induced structural changes of blood vessel.

1. Introduction

Personalized medicine initiatives aim to develop optimal cancer treatments that will direct patients towards "the right drug at the right dose at the right time" [1]. This is contingent upon not only personalized results of a highly specific/sensitive diagnostic test but also on assessing the effectiveness of the therapy post-administration. The cost of development of new drugs and treatments is estimated between $0.5–2 billion [2]. In order for such treatments to gain enough traction, preliminary effectiveness must be assessed with cost effective and readily available imaging tools. Conventional medical imaging is already in high demand and very expensive, making the addition of treatment monitoring within existing infrastructure a challenge [3]. In addition, imaging modalities commonly used to assess treatment efficacy become even more onerous when they are used on cancer patients for whom the physical and psychological toll of the treatment prohibits multiple imaging sessions. Often, contrast agents are required causing practical limitations to have the same patient imaged at multiple imaging timepoints after treatment [4,5]. There is a need for imaging modalities which are sensitive to early treatment-induced structural and functional changes. These technologies could generate imaging biomarkers to be used in conjunction with personalized medicine treatment regimens and therefore would provide a means for an oncologist to assess treatment response rapidly.

Quantitative ultrasound (QUS) [6–10] and Diffuse Optical Spectroscopy Imaging (DOSI) [11–15] are two promising modalities in early cancer treatment monitoring. QUS utilizes the frequency content of the ultrasound radiofrequency (US RF) signals to extract relevant information about the changes in the structural properties of cancer tumor tissue during treatment [8]. 2D parametric maps scatterer size and concentration can be constructed. Ongoing clinical studies have used textural characterization of QUS spectral parametric maps to differentiate treatment response with 100% sensitivity and 93% specificity 1 week after treatment [7]. Despite its successes, QUS is only capable of measuring the structural changes of tumor cell morphology that occur during treatment. Evidence suggests that these structural

* Corresponding author at: Department of Physics, Ryerson University, Toronto, M5 B 2K3, Canada.
E-mail address: mkolios@ryerson.ca (M.C. Kolios).

http://dx.doi.org/10.1016/j.pacs.2017.03.003

changes are dependent on tumor and treatment type and may not allow this technique to be robustly extended towards all cancer types [16]. Moreover, DOSI has shown that functional and metabolic changes (ex. hemoglobin concentration) may appear at earlier timepoints in patients with locally advanced breast cancer. An oxyhemoglobin flare has been reported 24 h post-treatment in responding patients due to the rapid increase in cellular metabolism from chemotherapeutic-induced cellular damage [11]. However, DOSI suffers from low spatial resolution rendering the anatomical localization of the metabolic changes difficult without assistance from external modalities such as MRI [15], or ultrasound and mammography [12]. Anatomical imaging must be merged with functional measures of tumor response for guiding therapy and avoiding an over-reliance on the "one-size-fits-all" conventional treatment and imaging approach.

Photoacoustic (PA) imaging has successfully mapped structural and functional aspects of biological tissue [17–21] such as neuronal functional connectivity [22], breast carcinoma patterns [23] and early detection of malaria [24]. Translation of PA imaging into the mainstream of clinical radiology requires well-suited clinical applications, most likely in combination with another anatomical imaging modality. Of particular importance is the similar nature of PA imaging with US whose images are naturally co-registered when the same transducers are used. Just as with the US RF signals in QUS, the frequencies of the PA signals carry information on the structure (size, shape and orientation) of the underlying absorber [25–27]. Recently published work has shown how QUS based on analysis of RF backscatter data can be used for biological tissue characterization of sub-resolution scattering structures [28]. In a similar manner, analysis of the PA radiofrequency signals has the potential of offering a system independent method of inferring sub-resolution tissue structural properties [29,30]. As red blood cells contained within vascular tissues generate the PA signal, the quantitative photoacoustic (QPA) method would be sensitive to the spatial distribution of RBCs contained within unresolved blood vessels (or locally hemorrhaged). This added sensitivity is of importance for pushing the sensitivity of acoustic resolution PA imaging beyond the resolution limit dictated by the transducer's bandwidth. Such advances would accelerate the clinical translation of PA imaging where clinically relevant ultrasound detection frequencies are used. In the past five years, several groups have employed the use of PA radiofrequency analysis to differentiate prostate adenocarcinoma tumors from normal tissue [31], detect the presence of red blood cell aggregation [30,32], identify various stages of liver disease [29,33] and characterize bone and joint microstructure in osteoporosis [34] and rheumatoid arthritis [35]. Theoretical models have also been developed for understanding the spectral features that arise from tissue microstructural changes [36–42]. Combining functional aspects of PA imaging (based on optical spectroscopy) with structural information (based on RF frequency analysis) can potentially be used to better monitor cancer treatment response.

The use of PA imaging for cancer treatment monitoring is a relatively new endeavor [43–45]. In this study, we correlate the spectral information of the PA RF data (QPA) with the oxygen saturation (sO_2) of in-vivo tumors treated with a novel thermosensitive liposome. The ultimate goal would be the development of robust quantitative imaging techniques capable of monitoring cancer treatments and predicting long term outcome. This will rely on the structural and functional changes that occur in tumor vasculature hours after the administration of treatment.

2. Methods

2.1. Animal model and treatment

Female, BALB/c mice (5–6 weeks old; 18–20 g) were purchased from Harlan Sprague Dawley Inc. (Mississauga, Canada). The left hind footpad of each animal was inoculated with 1×10^6 murine breast cancer (EMT-6, ATCC, Manassas, MA) cells in 50 μL DMEM medium. The tumor was grown for 7 days post-inoculation until a 1–2 mm increase in footpad thickness was measured. Animal protocols implemented in this study were approved by the Animal Care Committee of the University Health Network (Toronto, Canada) in accordance with the policies established by the Guide to the Care and Use of Experimental Animals (Canadian Council of Animal Care, Ottawa, Canada).

Treatment consisted of tail vein injections of the thermosensitive liposome containing doxorubicin (DOX) developed by our group (labeled Heat-activated cytoToxic – HaT-DOX) or control Saline. HaT-DOX preparation has been described elsewhere [46–49]. Briefly, DOX inside the 100 nm liposome was rapidly (<20 s) released at mild-hyperthermic temperatures (39–42 °C). HaT-DOX has shown improved release kinetics and tumor uptake relative to Lysolipid Temperature Sensitive Liposome (ThermoDox®, Celsion Corporation, Lawrenceville, NJ), which has progressed into late stage clinical trials for hepatocellular carcinoma [50,51].

HaT-DOX (10 mg DOX/kg) or Saline (HBS, pH = 7.4) was intravenously injected to 13 and 15 animals, respectively. The tumor-bearing footpad was then immediately placed in a water bath at 43 °C for 1 h under general anesthesia. The animals were separated into 3 groups based on post-treatment sacrifice timepoints: 2 h (HaT-DOX n = 3, Saline n = 4), 7 days (HaT-DOX n = 3, Saline n = 4) and beyond 7 days (HaT-DOX n = 7, Saline n = 7). Body weight and caliper measurements of the tumor thickness were recorded every few days until the study termination (28 days post-treatment) or at endpoints defined in the animal handling protocol.

Tumor histology was obtained for two imaging timepoints of interest, 2 h and 7 days post-treatment. Prior to sacrifice, an intravenous injection of FITC-lectin (0.25 mg/mL, 200 μL) was administered to 6 HaT-DOX treated animals and 8 Saline treated animals. This perfusion stain was allowed to circulate for 60 min before euthanizing the animals and surgically removing the tumors. Multiple sections were stained with H&E and DAPI for tumor cell localization and CD31 for endothelial cell presence. The FITC-lectin was used to establish the vessel structural integrity. Image analysis and quantification of each stain was performed using Definiens software (Definiens, Munich, Germany) at the STTARR facility (University Health Network, Toronto, Canada).

2.2. Longitudinal US and PA imaging

Co-registered US and PA images of the tumors were obtained longitudinally. The Vevo LAZR system (Fujifilm VisualSonics Inc., Toronto, Canada) was used to acquire 3D images at 40 MHz using a 256 element linear array transducer. The coaxial US cable and optical fiber bundle were integrated in a special enclosure [52]. The fiber bundle delivered wavelengths (680–970 nm) from an optical parametric oscillator (20 Hz repetition rate) coupled to a tunable Nd:YAG laser (30 mJ per pulse, 10 ns pulse length). The optical fiber bundle bifurcated into two 14×1.25 mm rectangular strips 30° relative to the imaging plane. With the PA imaging mode on the system, US acquisition was synchronized with the laser output to ensure image co-registration.

Anesthetized mice were placed prone on a heating platform at 37 °C. Clear, ultrasound gel acoustically coupled the tumor with the US/PA probe. Imaging was performed at six timepoints: 30 min

pre-treatment (Pre tx), 30 min post-treatment (30 min post tx), 2 h post-treatment (2 h post tx), 5 h post-treatment (5 h post tx), 24 h post-treatment (24 h post tx) and 7 days post-treatment (7d post tx). At each timepoint, 3D US/PA data were acquired by mechanically scanning (80 μm step size) the transducer to cover the entire tumor volume. For each step, a 2D B-mode image was beamformed using 4 laser pulses at 750/850 nm at 5 Hz frame rate. The energy of the beam was monitored in real time. A total of 81 2D, US and PA frames were acquired for each animal at each imaging timepoint.

Reference phantoms were used to remove the system dependencies and compute spectral parameters using techniques developed in QUS [53,54]. The US reference phantom was constructed with glass beads (diameter 6.15 ± 1.15 μm, Potters Industries, Parsippany, NJ, US) in a gelatin background [55]. The top of the phantom was covered with 128 μm TPX® (Matsui Chemicals America, Inc., Rye Brook, NY, USA) for its tissue-like acoustic impedance [56]. The acoustic properties were measured using single element transducers (1541 m/s speed of sound; 0.723 dB/cm attenuation at 40 MHz). The PA reference counterpart contained black, carbon spheres (diameter 1–12 μm) suspended in a gelatin background with similar acoustic properties to the US phantom [57]. Both reference phantoms were imaged at the end of each day using exacty the same settings as those used for the tumors.

2.3. sO_2/QUS/QPA signal processing

A schematic of the signal processing that is performed using the US and PA tumor images are shown in Fig. 1. The US/PA datasets at every timepoint were considered to be functions of tumor spatial location, (x, y, z) and optical wavelength of illumination, λ for PA imaging. The z direction refers to the transducer scanning direction over the entire tumor volume. In the temporal/spatial domain, the analysis region of interest (ROI) for the tumor was chosen by creating a spatial mask obtained by manual segmentation of the tumor for the US images:

$$\begin{aligned} u(x,y,z)_{tumor} &= u_0(x,y,z) \times m(x,y,z) \\ p(x,y,z,\lambda)_{tumor} &= p_0(x,y,z,\lambda) \times m(x,y,z) \end{aligned} \quad (1)$$

where, $u_0(x, y, z)$ and $p_0(x, y, z, \lambda)$ are the US and PA images obtained within the entire field of view of the transducer, respectively; $m(x, y, z)$ is the binary mask that contains the tumor ROI which was obtained from the manual segmentation.

In order to compute the oxygen saturation (sO_2) of the tumor, segmented PA images were normalized by the energy of the two laser wavelengths of illumination, 750 and 850 nm. No fluence corrections were performed due to the complexity of accounting for the effect of wavelength dependent optical extinction on light propagation in heterogeneous tumor tissue. Here we directly use the PA amplitude ratio between 750 nm and 850 nm to relate to oxygen saturation and how these change as a function of treatment time, without compensation for local fluence variations. For this reason, changes in relative sO_2 values were analyzed rather than absolute values. The effect of fluence correction on sO_2 estimations has been previously reported, particularly its effect on depths greater than 5 mm [58,59]. The PA signal amplitude, $p_{SA}(x, y, z, \lambda)$ was calculated by computing the envelope of the time-domain PA signals within the region of interest. The sO_2 for each 2D slice was then calculated using the two-wavelength approach [60]:

$$sO_2(x,y,z) = \frac{p_{SA}(x,y,z,\lambda_2)\varepsilon_{Hb}(\lambda_1) - p_{SA}(x,y,z,\lambda_1)\varepsilon_{Hb}(\lambda_2)}{p_{SA}(x,y,z,\lambda_1)\Delta\varepsilon(\lambda_2) - p_{SA}(x,y,z,\lambda_2)\Delta\varepsilon(\lambda_1)} \quad (2)$$

where, Hb refers to deoxygenated hemoglobin, $\varepsilon_{Hb}(\lambda)$ is the molar extinction coefficient of deoxygenated hemoglobin at wavelength λ, and $\Delta\varepsilon(\lambda)$ is the difference between the extinction coefficient of oxygenated hemoglobin (HbO) and its deoxygenated

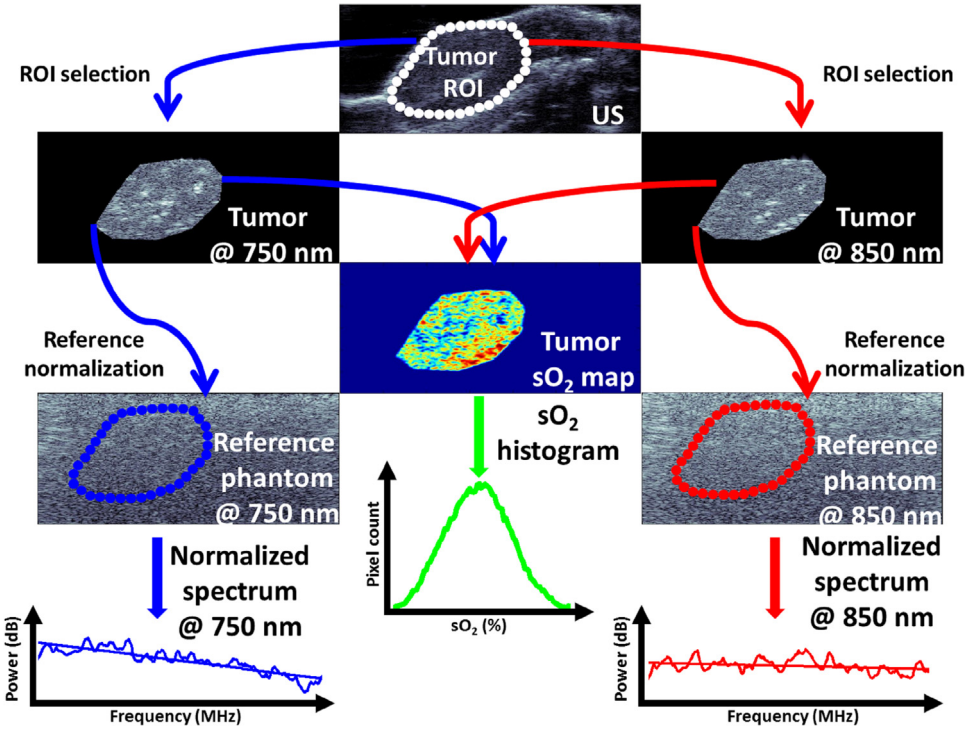

Fig. 1. Schematic for generating tumor oxygenation maps and PA spectral parameters. The ROI segmented from the US images is applied to the co-registered PA images at 750 and 850 nm which are then used to generate a tumor sO_2 map. Oxygenation histograms of every slice within the tumor provide a quantitative distribution of sO_2 values from which the average mode is calculated. The ROI mask is also applied to the reference phantoms at both wavelengths. The frequency information of the PA phantoms is subtracted from the tumor RF spectra and the normalized power spectra are used to retrieve the spectral parameters. For the US normalized spectra, the US image and reference phantom is used to obtain the same parameters.

counterpart at λ. In this case, λ_1 and λ_2 correspond to 750 and 850 nm, respectively. Once the sO_2 value for every point in the images was computed, histograms of the distributions of sO_2 values, $H(sO_2)$ were calculated. The average mode (i.e. most commonly occurring sO_2 value) was retrieved for all segmented slices within the tumor and all mice at that particular timepoint and treatment group,

$$Mode[sO_2] = \frac{1}{MS}\sum_{i=1}^{M}\sum_{j=1}^{S} mod\left(H_{ij}(sO_2)\right) \quad (3)$$

where, M and S represent the number of mice and slices, respectively.

To compute the US and PA spectral parameters as a function of time post-treatment, the average, normalized power spectrum (PS_{norm}) was computed by removing the system dependencies through the use of the reference phantom technique developed for QUS [9]:

$$PS_{normUS}(f,z) = \frac{1}{S}\sum_{i=1}^{S}\log_{10}\left(\frac{U(f,z_i)_{tumor}}{U(f,z_i)_{ref}}\right)^2 \quad (4)$$

where, $U(f, z)_{tumor}$ and $U(f, z)_{ref}$ are the average, $z-th$ slice US power spectra for the tumor and US reference phantom in the axial dimension and averaged in the lateral dimension (at least 100 RF lines per segmentation, depending on the size of the tumor). Similarly, the average PA power spectra for the tumor and the PA reference phantom can be written as:

$$PS_{normPA}(f,z,\lambda) = \frac{1}{S}\sum_{i=1}^{S}\log_{10}\left(\frac{P(f,z_i,\lambda)_{tumor}}{P(f,z_i,\lambda)_{ref}}\right)^2 \quad (5)$$

where, $P(f, z, \lambda)$ is the Fourier Transform of the PA signals for the tumor and reference.

The US and PA normalized spectra were fitted to a straight line within the −6 dB bandwidth of the transducer (25–40 MHz in this case) in order to extract the spectral parameters [61,62]. The spectral slope was extracted from:

$$PS_{fit}(f) = SS \times f + Y_{int} \quad (6)$$

where, PS_{fit} is the result of performing linear regression on either $PS_{normUS}(f, z)$ or $PS_{normPA}(f, z, \lambda)$, SS is the spectral slope measured in dB/MHz and Y_{int} is the y-intercept of the fit measured in dB. An additional parameter, the midband fit (MBF), a measure of scattering strength, was assessed by measuring the power spectrum amplitude in the middle of the bandwidth used for the analysis of the signals. The goal was to extract QUS/QPA parameters that could be used to monitor the structural aspects of the HaT-DOX treatment, namely changes in the size and concentration of optical absorbers.

3. Results and discussion

3.1. Treatment efficacy

The progression of tumor size after the administration of the HaT-DOX and Saline treatments is shown in Fig. 2. Each animal treated with HaT-DOX was classified as a responder if the tumor size showed a relative decrease of >50% at study termination [63]. An overall reduction in tumor size was observed for all HaT-DOX treated animals except a single non-responder which exhibited a 100% increase in tumor size 21 days post-treatment. This non-responder mouse was treated in an identical fashion and was included in this data set as its oxygenation and QUS/QPA behavior was significantly different from HaT-DOX responders. As reported in our previous study for a larger subset of animals, a 90% regression rate was observed 25 days after HaT-DOX treatment [43].

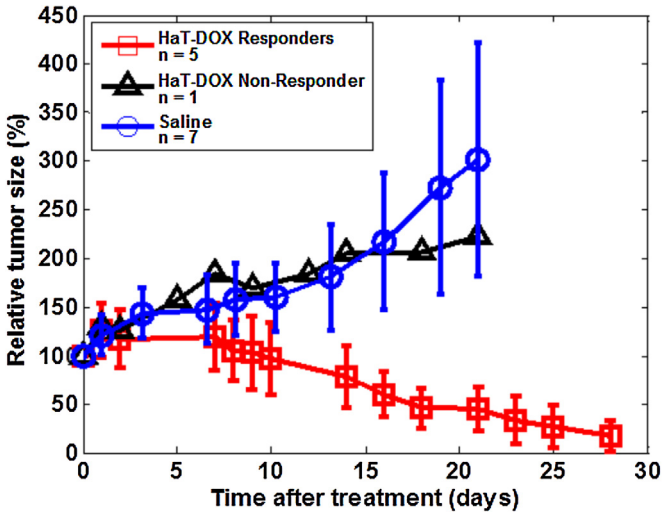

Fig. 2. Average, relative tumor growth as a function of time post-treatment. Each point represents the average and standard deviation (error bars) of the relative tumor size for 6 HaT-DOX treated mice and 7 Saline control mice. The HaT-DOX non-responder and the Saline control animals were euthanized at day 21.

Thermosensitive liposomes eliminate the systemic toxicity associated with chemotherapeutic drugs such as DOX [49]. The effectiveness of the HaT-DOX treatment was evident when compared to the Saline control group, whose tumors increased 200% in size. For the first 10 days post-treatment, the behavior of the two groups was similar. Although not independently assessed, this was likely due to transient inflammation of the footpad upon DOX release [50]. As the inflammation subsided, rapid tumor regression was observed in the HaT-DOX group and by 28 days, normal footpad appearance and function (e.g. gripping) was restored. This is consistent with previous studies where the efficacy of HaT-DOX has been studied extensively [48,49]. The variation in tumor size for the Saline group was significantly larger than for HaT-DOX. This could be a result of the random distribution of blood vessels in untreated tumors which leads to variable tumor growth rates [64] and arises as a result of the lack of DOX-induced vascular shutdown [65].

3.2. HaT-DOX tumor oxygenation and PA normalized power spectra

In order to examine the changes in the oxygenation of the tumor vasculature after the administration of the HaT-DOX formulation, average sO_2 histograms were plotted for the pre-treatment and at the 2 h/24 h/7d post-treatment imaging time-points (Fig. 3a). These animals all responded to the HaT-DOX treatment (as assessed by caliper measurements) and experienced a 2 h post-treatment, 22% drop in oxygenation (as assessed by the sO_2 mode). This drop in oxygenation was present as early as 30 min post-treatment and was sustained for the first 24 h. Tumor oxygenation histograms can be used to quantify changes in blood vessel oxygenation throughout the entire tumor [43]. The early changes in blood vessel oxygenation correlate with treatment response: responders' sO_2 decreased 30 mins post-treatment.

The PA PS_{norm} are shown for the same timepoints as the sO_2 histograms to investigate whether the change in oxygenation is accompanied by a physical change in vascular structure (Fig. 3b). At the middle of the transducer bandwidth (i.e. midband fit or MBF), an increase of 6.2 dB is observed for the 750 nm PS_{norm} at the 2 h timepoint relative to pre-treatment; at 850 nm this increase was 2 dB. These changes persisted for the first 5 h post-treatment. By

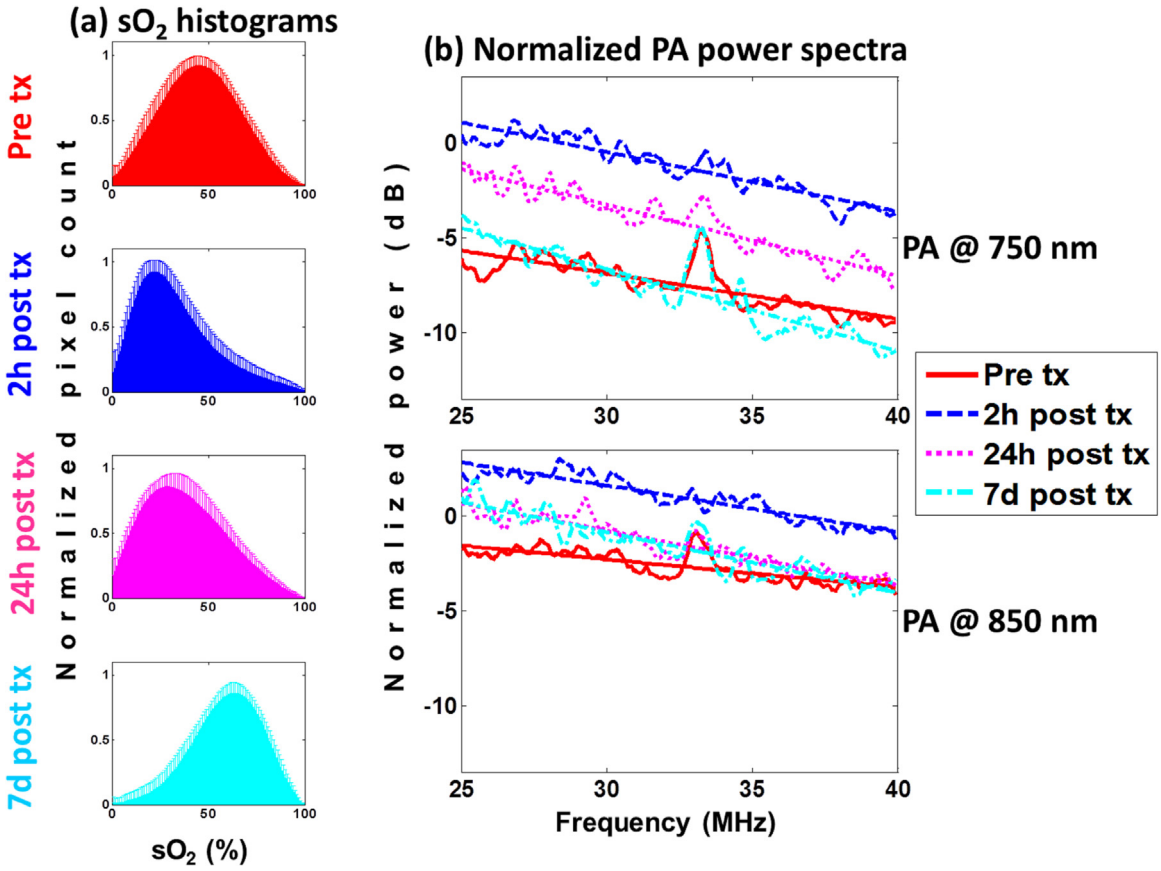

Fig. 3. HaT-DOX-treated mice (a) tumor oxygenation histograms and the (b) normalized power spectra for PA images obtained at 750 (top) and 850 nm (bottom) for multiple imaging timepoints. The error bars on the histograms represent the standard deviation on the pixel count for each sO_2 value obtained from 21 different histograms per timepoint per mouse. The power spectra are averages of at least 100 RF lines per 21 tumor slices per timepoint (6 total) per mouse (5 total). All linear regressions had a Chi-squared value ≥0.9. Treatment is abbreviated as tx.

24 h post-treatment, the PS_{norm} amplitude approached pre-treatment levels, and by 7d post-treatment it decreased by 3.4 dB relative to the value at 2 h for 750 nm.

Changes in the MBF are known to correlate to changes in the concentration of optical absorbers [30,31,66]. The frequency content of the PA signals may also contain information about the absorber concentration. Provided that the optical absorption within the tumor is strong, the decay of the light fluence inside the tumor may alter the frequency content of the RF signal. Differences in signal strength between the two wavelengths arise from the changes in vessel oxygenation. Treatment-induced vascular collapse leads to the hypothesis that oxygenation decreases at the early timepoints. Therefore, it is expected that the PA signal at 750 nm would be higher than for 850 nm, as predicted from the optical absorption spectra of oxygenated and deoxygenated hemoglobin. By 7d post-treatment, the sO_2 of the blood vessels increased by over 20% compared to pre-treatment (Fig. 3a). This resulted in the 7d, 750 nm MBF decrease suggesting that the MBF can differentiate between two different states of vessel oxygenation.

3.3. Saline tumor oxygenation and PA normalized power spectra

The sO_2 histograms for the Saline-treated mice are shown in Fig. 4a. Unlike their HaT-DOX counterparts, no significant changes in oxygenation were measured. The sO_2 histograms at 2 h post-treatment appear wider than pre-treatment but the histogram mode did not change. This could be due to significant variability within the oxygenation and tumor size (Fig. 2). Mice with a low pre-treatment sO_2 did not undergo changes post-treatment, while others increased. At the 7d timepoint, the average oxygenation of the tumor increased by 20% relative to oxygenation values pre-treatment.

The PA PS_{norm} for this group did not significantly change compared to pre-treatment (Fig. 4b). At 7d, the 750 nm MBF decreased by 3.2 dB. The lack of changes in the early timepoints suggested that the Saline treatment did not induce the same vascular changes in the tumor as HaT-DOX. The decrease of the MBF at 7d is correlated to a 20% increase in the sO_2 of blood vessels thought to occur due to the recruitment of vessels required to maintain tumor growth [64].

3.4. Correlation of QPA spectral parameters with tumor oxygenation

The sO_2 mode was plotted against the PA spectral slope (SS) for HaT-DOX responders, the lone HaT-DOX non-responder and the Saline-treated mice (Fig. 5). At each timepoint, the SS and sO_2 mode is represented by the average value across all mice within a treatment group. A total of 21 planes were analyzed to examine the distribution of metrics across the entire tumor volume. The clustering of HaT-DOX responders by imaging timepoint was clear for both wavelengths (Fig. 5a). The PA SS at 750 and 850 nm decreased by 45% and 73%, respectively when the sO_2 mode dropped at 30 min post-treatment. These changes in SS persist for the first 24 h post-treatment until the oxygenation of the tumors increased by 10% from 30 min. During this interval, the SS further decreased by 8.5% and 11.5% for 750 and 850 nm, respectively. By 7d post-treatment, an increase in the average sO_2 mode of 22%

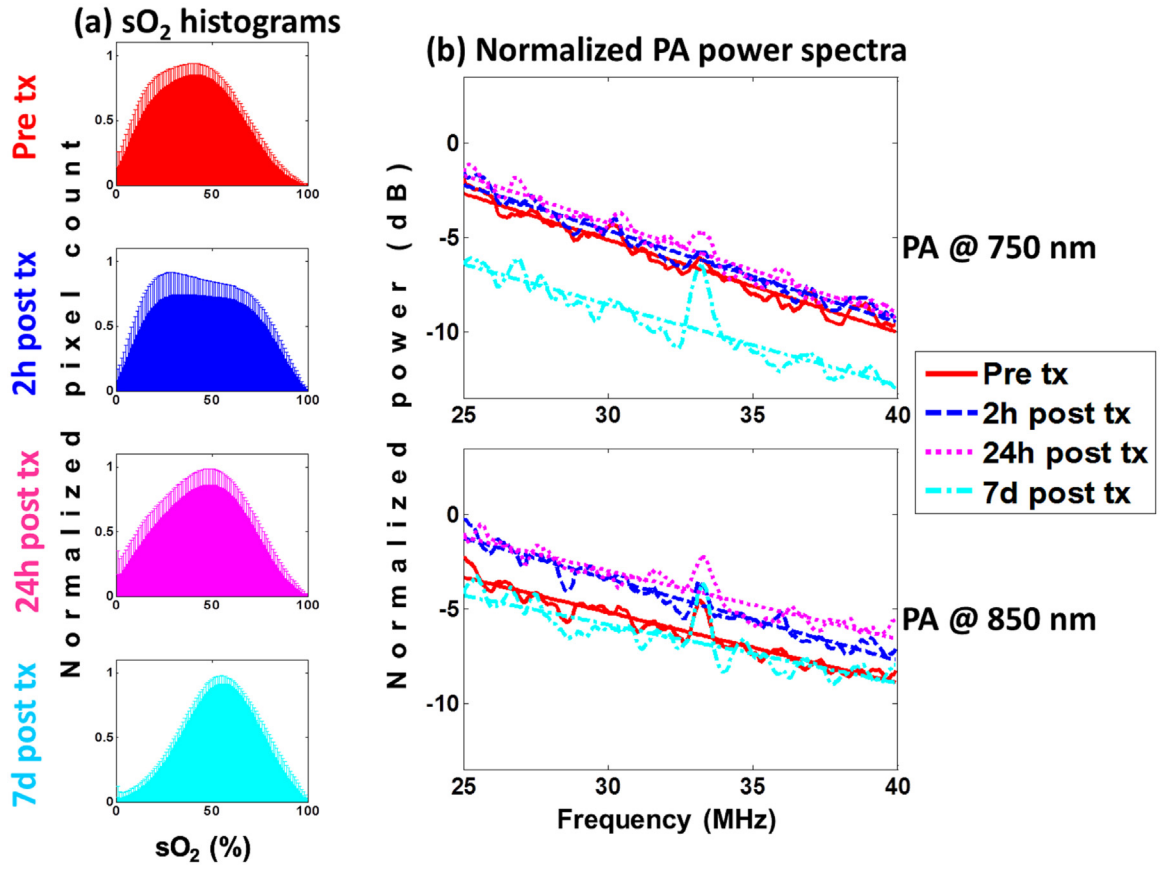

Fig. 4. Saline-treated mice (a) tumor oxygenation histograms and the (b) normalized power spectra for PA images obtained at 750 (top) and 850 nm (bottom) for multiple imaging timepoints. The error bars on the histograms represent the standard deviation on the pixel count for each sO_2 value obtained from 21 different histograms per timepoint per mouse. The power spectra are averages of at least 100 RF lines per 21 tumor slices per timepoint (6 total) per mouse (7 total). All linear regressions had a Chi-squared value $\geq$0.9. Treatment is abbreviated as tx.

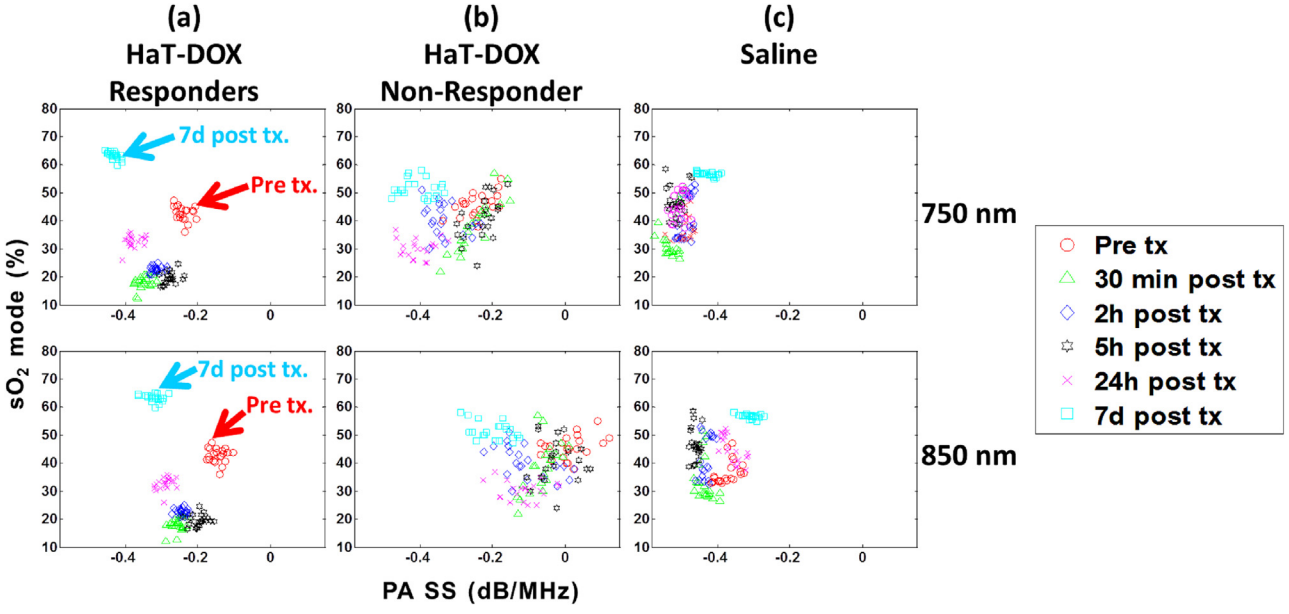

Fig. 5. Oxygen saturation (sO_2) mode versus the PA spectral slope (PA SS). The PA SS is computed for 750 nm (top row) and 850 nm (bottom row) and for HaT-DOX (a) responders (n = 5) and (b) non-responder (n = 1) and (c) Saline (n = 7). Each dot represents the average SS across at least 100 PS_{norm} within 21 tumor slices per timepoint, per mouse.

from pre-treatment was accompanied by a decrease of the SS (79% for 750 nm and 113% for 850 nm). PA estimates of tumor oxygen saturation reported here are also described in other reports. Mallidi and colleagues have used the VevoLAZR system to track the progression of photodynamic therapy and found tumor sO_2 values to be around 40–60% before and after the administration of vascular disrupting therapies [44]. In a more recent report, Rich and Seshandri reported good correlations between PA estimates of sO_2 with oxygen-enhanced magnetic resonance imaging in head and neck xenograft tumors [67]. Additionally, PA estimates of sO_2 reported here have also been previously correlated with hypoxia stains obtained from tumor sectioning and were found to adequately represent the tumor microenvironment [68].

The HaT-DOX non-responder (Fig. 5b) does not exhibit the same behavior as the HaT-DOX responders. Vessel oxygenation did not significantly drop 24 h post-treatment and a higher variation in the distribution of SS values was observed throughout the imaging timepoints. Furthermore, there were no identifiable trends in the SS during treatment other than a 0.2 dB/MHz difference in the PA SS for 850 nm compared to 750 nm observed at all imaging timepoints for this mouse.

The Saline SS exhibited a distinctive behavior, differentiating them from the HaT-DOX mice (Fig. 5c). The 750 nm SS did not significantly change at the early timepoints as shown by the clustering around −0.48 dB/MHz. This was also correlated with the lack of sO_2 changes at early timepoints. The 850 nm SS increased by 14% from pre-treatment when the sO_2 increased 20% at the 7d timepoint. For the 850 nm illumination, the SS increased slightly (3%) at the 24 h timepoint before increasing by 16% at 7d post-treatment. Overall, the 850 nm SS is ∼0.1 dB/MHz higher than 750 nm and lower than the HaT-DOX SS. The significance of these findings can be established by examining the correlation between the SS and the optical absorber (i.e. vascular morphology) [30,41]. The lack of large changes in the SS for the Saline and HaT-DOX non-responder implies that the tumor vasculature is responding differently to treatments. It is worth noting that the differences in the SS trends post-treatment are sufficient to identify the non-responder and the control group.

3.5. Histological examinations post-treatment

Representative cross-sections of tumors extracted after the 2 h imaging timepoint are shown in Fig. 6. A large amount of FITC-lectin leakage was observed in the of vicinity blood vessels (Fig. 6a). Overall, 70% of all vessels within the HaT-DOX-treated tumor were FITC-lectin positive compared to just 30% for the Saline treatment at 2 h (Fig. 6b). Fig. 6c shows the distribution of vessel size within the tumor measured 2 h post-treatment. The Saline group had a larger number of intact vessels post-treatment compared to the HaT-DOX group, except for vessels smaller than 25 μm.

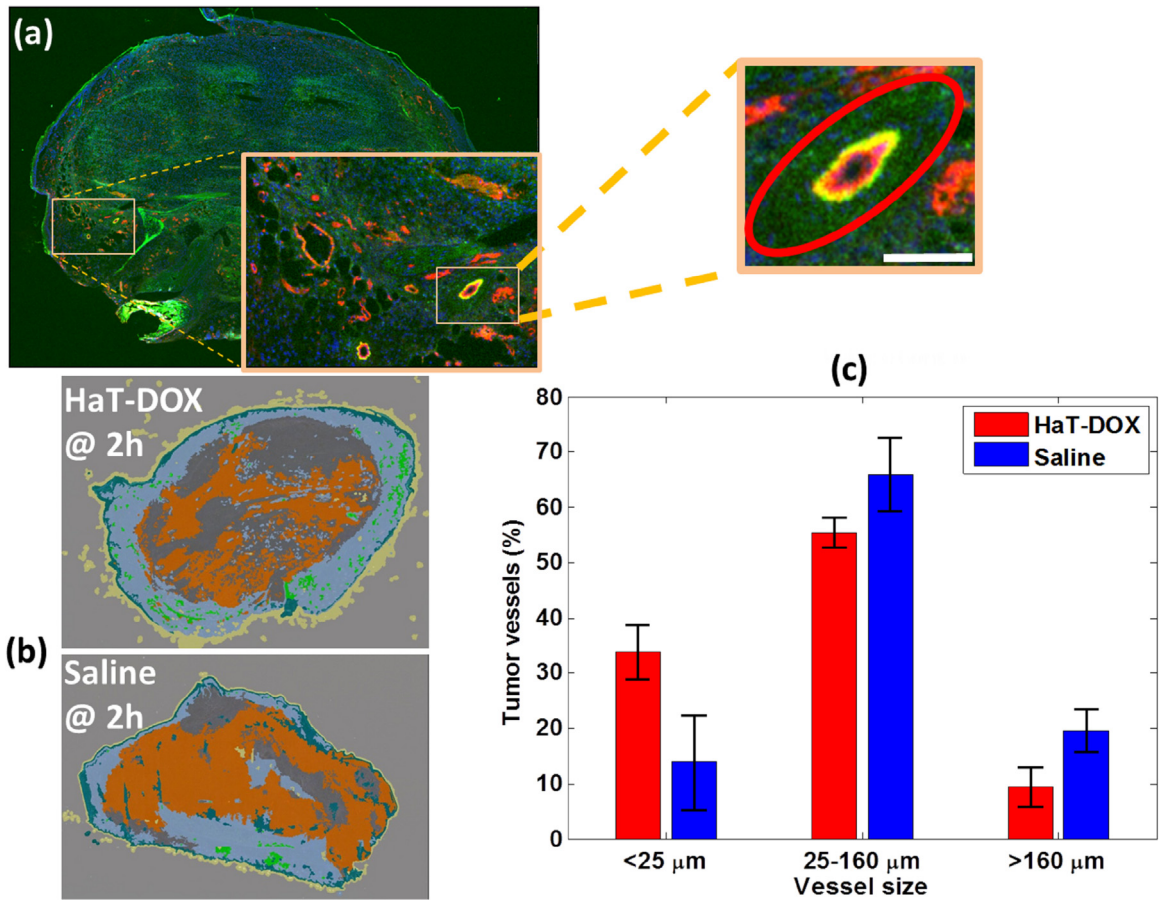

Fig. 6. Tumor histology obtained 2 h post-treatment. (a) Representative images of HaT-DOX-treated tumor blood vessels (2 h post-treatment) stained with CD-31 (red and yellow) showing the leakage of FITC-lectin (green) in their vicinity (red ellipse). The width of the image is 10 mm and the scale-bar in the zoomed inset is 100 μm. (b) Representative HaT-DOX and Saline tumors showing the proportion of FITC-lectin leakage (dark gray) outside of the tumor area (orange). Normal tissue is the teal color surrounding the tumor and the slide background is light gray. For more details on how these images were obtained refer to reference [43]. (c) Distribution of the size of tumor blood vessels for HaT-DOX and Saline measured at the 2 h timepoint.

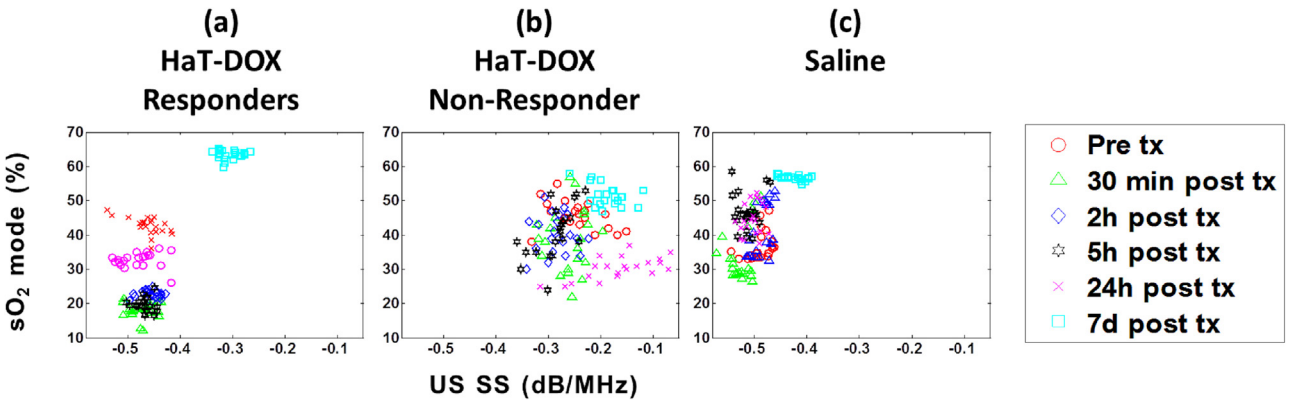

Fig. 7. The correlation between US SS and sO_2 mode for HaT-DOX (a) responders and (b) non-responder and (c) Saline. Each dot represents the average SS across at least 100 RF spectra within 21 tumor slices per timepoint per mouse.

The mechanism of action for treatments like HaT-DOX is the rapid (<20 s), burst-release of DOX upon exposure to mild-hyperthermia [69,70]. The formation of large DOX concentration gradients from the tumor vasculature to the tumor interstitial space leads to DOX-induced endothelial cell damage. The damaged endothelial cells become unable to support the circulating blood and its contents, eventually succumbing to hemorrhage, blood coagulation, pooling and localized vascular shutdown [65,71]. This phenomenon was observed in Fig. 6a and b for tumors treated with HaT-DOX.

The recently published study by our group examined the correlation between sO_2 and vascular damage due to a single dose of HaT-DOX released during mild-hyperthermia [43]. At the 2 h timepoint, the drop in sO_2 was correlated with an increase in FITC-lectin leakage within the tumor interstitium. At 750/850 nm, the most dominant optical absorber is RBC' hemoglobin [60]. Given the significant amount of FITC in the vicinity of post-treatment blood vessels (Fig. 6a), treatment leads to an increased number of leaked RBCs in the interstitium, where they are no longer capable of circulating and unable to exchange pulmonary oxygen, and so eventually become deoxygenated. We hypothesize that this contributes to the post-treatment decrease in tumor oxygenation (Fig. 3a). Furthermore, the hemorrhage of RBCs in the intersitium of tumors inadvertently forms an optical target with the same absorption properties as RBCs but larger effective size (i.e. RBCs are no longer confined to the blood vessels). The formation of this "pool" of RBCs outside the vessels may be responsible for the changes in the spectral slope shown in Fig. 5a. Previous experimental studies by our group and others have demonstrated that an increase in the effective optical absorber size causes a decrease in the PA SS [30,32,57,66,72]. Moreover, this trend was also confirmed in a simulation study which examined the effect of vascular hemorrhaging on the QPA SS parameter [42]. By 7 days post-treatment, both groups had sufficient time to recruit and generate new blood vessels. The effects of re-vascularization following cancer treatments have been previously studied using other modalities [11–13] and are consistent with the observed increase in tumor sO_2 reported in the current study at 7 days.

The post-treatment changes in the PA SS at both wavelengths are expected to be dependent on the size of vessels inside the tumor post-treatment as compared to pre-treatment. Changes in the distribution of tumor vessels are shown in Fig. 6c. This is consistent with the experimental results: the PA SS of the Saline group was more negative than for the HaT-DOX group (Fig. 5c). Additionally, the sub-resolution sized vessels were found to be more abundant in the HaT-DOX treated group. Although smaller than the system spatial resolution (axial 45 μm, lateral 90 μm) the PA signal from collections of these vessels can contribute to the recorded RF PA signal and the SS. This is a phenomenon that is observed during studies of acoustic-resolution PA imaging where speckle dominates the images due to collections of unresolved sources of PA waves [29,57,74].

3.6. Quantitative ultrasound for detecting tumor cell death

In order to compare the treatment monitoring capabilities of QPA with quantitative ultrasound (QUS), the SS from the US imaging of the tumors was computed for all the imaging timepoints and treatments (Fig. 7). It is evident that QUS is unable to identify changes in the structure of the tumor as early as a few hours post-treatment in the same manner as the PA SS. The US SS does not significantly change in HaT-DOX treated tumors until the 7d timepoint despite the large drop in oxygenation (Fig. 7a). At 7d, the US increased by nearly 35%, which is indicative of a decrease in the size of the scatterers (i.e. tumor cells seen) due to the structural changes that the tumor has undergone. No noticeable trend was observed in the SS of the HaT-DOX non-responder (Fig. 7b). The SS of the Saline control (Fig. 7c) increased by 24% at 7d compared to pre-treatment. It is important to note that by 7d there were no significant changes in the size of the tumors between all groups, as assessed through caliper measurements (Fig. 2).

The examination of the changes that the tumor cells undergo during and after treatment is another aspect of treatment monitoring. QUS has been successful in probing the structural changes that occur within tumor cells when they are exposed to changing environmental conditions [75–77]. Recently, the technique was used to evaluate the treatment response of breast and prostate cancer patients before conventional imaging modalities [6–8]. However, the technique is sensitive to localized changes in the structure of the tumor cells and cannot provide functional information on the tumor vasculature in the same manner as PA imaging. Additional complexity arises from the fact that inflammation of the tumors was present one week after treatment. This could complicate interpretation of results, as changes in the acoustic properties of the tumor microenvironment have been shown to affect QUS parameters such as the SS [78]. This renders the interpretation of changes in parameters more challenging than in QPA where the specific, oxygen dependent optical absorption of hemoglobin is known to dominate the PA signal generation. Therefore, there is a more direct link to the relation between the changes detected in the PA signals collected and how these can be interpreted based on the underlying biophysical changes in tissue structure that occur because of the treatment. The latter is an

important consideration in using QPA for monitoring vascular-targeted therapies.

4. Conclusions

Our study demonstrates the potential of using PA imaging and QPA for monitoring treatment-induced changes in the tumor vasculature. Changes in quantitative photoacoustics as early as 30 min post-treatment are strongly correlated with a significant drop in oxygenation observed at the same timepoints. These correlated values continue through to 5 h where they are shown to correlate with changes to the vasculature as observed via histology. In fact, the spectral analysis of the PA RF data provides evidence for the loss of oxygenation due to HaT-DOX-induced vascular destruction. Our results indicate that the frequency content of the PA data provides useful information related to the changes in the morphology of blood vessels during treatment. Comparisons with QUS suggest that the QPA technique is capable of identifying treatment responders as early as a few hours post-treatment for treatments that disrupt the vasculature. This study establishes the feasibility of using PA imaging and spectroscopy for treatment monitoring and should be used to assist with the translation of PA imaging to mainstream radiology.

Acknowledgments

Funding for this project was provided in part by the generous financial support of the Terry Fox Foundation, the Natural Sciences and Engineering Research Council of Canada (NSERC), the Canada Research Chairs Program, the Ontario Institute for Cancer Research and the Canadian Institutes for Health Research (CIHR). EH is supported by an NSERC Vanier Canada Graduate Scholarship. SDL is supported by the Prostate Cancer Foundation and CIHR Young Investigator Awards. We would like also to acknowledge the technical support received by the STTARR facility at the University Health Network and Fujifilm-Visual Sonics.

References

[1] M.A. Hamburg, F.S. Collins, The path to personalized medicine, N. Engl. J. Med. 363 (4) (2010) 301–304.
[2] C.P. Adams, V.V. Brantner, Estimating the cost of new drug development: is it really $802 million? Health Aff. (Millwood) 25 (2) (2006) 420–428.
[3] J.H. Thrall, Personalized medicine1, Radiology 231 (June (3)) (2004) 613–616.
[4] D. Gonzalez de Castro, P.A. Clarke, B. Al-Lazikani, P. Workman, Personalized cancer medicine: molecular diagnostics, predictive biomarkers, and drug resistance, Clin. Pharmacol. Ther. 93 (June (3)) (2013) 252–259.
[5] J.J. Smith, A.G. Sorensen, J.H. Thrall, Biomarkers in imaging: realizing radiology's future, Radiology 227 (3) (2003) 633–638.
[6] A. Sadeghi-Naini, et al., Quantitative ultrasound spectroscopic imaging for characterization of disease extent in prostate cancer patients, Transl. Oncol. 8 (1) (2015) 25–34 (Feb).
[7] A. Sadeghi-Naini, et al., Early prediction of therapy responses and outcomes in breast cancer patients using quantitative ultrasound spectral texture, Oncotarget 5 (May (11)) (2014) 3497–3511.
[8] A. Sadeghi-Naini, et al., Quantitative ultrasound evaluation of tumor cell death response in locally advanced breast cancer patients receiving chemotherapy, Clin. Cancer Res. Off. J. Am. Assoc. Cancer Res. 19 (April (8)) (2013) 2163–2174.
[9] H. Tadayyon, et al., Quantitative ultrasound assessment of breast tumor response to chemotherapy using a multi-parameter approach, Oncotarget (April) (2016).
[10] L. Sannachi, et al., Non-invasive evaluation of breast cancer response to chemotherapy using quantitative ultrasonic backscatter parameters, Med. Image Anal. 20 (February (1)) (2015) 224–236.
[11] D. Roblyer, et al., Optical imaging of breast cancer oxyhemoglobin flare correlates with neoadjuvant chemotherapy response one day after starting treatment, Proc. Natl. Acad. Sci. U. S. A. 108 (August (35)) (2011) 14626–14631.
[12] D.B. Jakubowski, et al., Monitoring neoadjuvant chemotherapy in breast cancer using quantitative diffuse optical spectroscopy: a case study, J. Biomed. Opt. 9 (February (1)) (2004) 230–238 (Feb).
[13] A. Cerussi, et al., Predicting response to breast cancer neoadjuvant chemotherapy using diffuse optical spectroscopy, Proc. Natl. Acad. Sci. U. S. A. 104 (March (10)) (2007) 4014–4019.
[14] W.T. Tran, et al., Multiparametric monitoring of chemotherapy treatment response in locally advanced breast cancer using quantitative ultrasound and diffuse optical spectroscopy, Oncotarget (March) (2016).
[15] R. Choe, et al., Diffuse optical tomography of breast cancer during neoadjuvant chemotherapy: a case study with comparison to MRI, Med. Phys. 32 (4) (2005) 1128–1139 (Apr).
[16] F.D.S.E. Melo, L. Vermeulen, E. Fessler, J.P. Medema, Cancer heterogeneity—a multifaceted view, EMBO Rep. 14 (8) (2013) 686–695.
[17] L.V. Wang, S. Hu, Photoacoustic tomography: In vivo imaging from organelles to organs, Science 335 (March (6075)) (2012) 1458–1462.
[18] S.Y. Emelianov, P.-C. Li, M. O'Donnell, Photoacoustics for molecular imaging and therapy, Phys. Today 62 (8) (2009) (p. 34).
[19] P. Beard, Biomedical photoacoustic imaging, Interface Focus 1 (August (4)) (2011) 602–631.
[20] Y. Jin, C. Jia, S.-W. Huang, M. O'Donnell, X. Gao, Multifunctional nanoparticles as coupled contrast agents, Nat. Commun. 1 (4) (2010) 1–8.
[21] A. Taruttis, S. Morscher, N.C. Burton, D. Razansky, V. Ntziachristos, Fast multispectral optoacoustic tomography (MSOT) for dynamic imaging of pharmacokinetics and biodistribution in multiple organs, PLoS One 7 (Januarr (1)) (2012) e30491.
[22] M. Nasiriavanaki, J. Xia, H. Wan, A.Q. Bauer, J.P. Culver, L.V. Wang, High-resolution photoacoustic tomography of resting-state functional connectivity in the mouse brain, Proc. Natl. Acad. Sci. 111 (1) (2014) 21–26.
[23] M. Heijblom, et al., Photoacoustic image patterns of breast carcinoma and comparisons with Magnetic Resonance Imaging and vascular stained histopathology, Sci. Rep. 5 (2015) p. 11778.
[24] C. Cai, et al., In vivo photoacoustic flow cytometry for early malaria diagnosis, Cytom. J. Int. Soc. Anal. Cytol. (April) (2016).
[25] G.J. Diebold, M.I. Khan, S.M. Park, Photoacoustic 'signatures' of particulate matter: optical production of acoustic monopole radiation, Science 250 (October (4977)) (1990) 101–104.
[26] E.M. Strohm, E.S.L. Berndl, M.C. Kolios, Probing red blood cell morphology using high-Frequency photoacoustics, Biophys. J. 105 (1) (2013) 59–67.
[27] E.M. Strohm, I. Gorelikov, N. Matsuura, M.C. Kolios, Modeling photoacoustic spectral features of micron-sized particles, Phys. Med. Biol. 59 (19) (2014) 5795–5810.
[28] Quantitative Ultrasound in Soft Tissues, in: J. Mamou, M.L. Oelze (Eds.), Springer Netherlands, Dordrecht, 2013.
[29] G. Xu, et al., The functional pitch of an organ: quantification of tissue texture with photoacoustic spectrum analysis, Radiology 271 (January (1)) (2014) 248–254.
[30] E. Hysi, R.K. Saha, M.C. Kolios, Photoacoustic ultrasound spectroscopy for assessing red blood cell aggregation and oxygenation, J. Biomed. Opt. 17 (12) (2012) 125006–125006.
[31] R.E. Kumon, C.X. Deng, X. Wang, Frequency-domain analysis of photoacoustic imaging data from prostate adenocarcinoma tumors in a murine model, Ultrasound Med. Biol. 37 (5) (2011) 834–839.
[32] E. Hysi, R.K. Saha, M.C. Kolios, On the use of photoacoustics to detect red blood cell aggregation, Biomed. Opt. Express 3 (9) (2012) 2326–2338.
[33] X. Wang, et al., Photoacoustic physio-chemical analysis of liver conditions in animal and human subjects, Proc. SPIE vol. 9708 (2016) p. 97081K–97081K–6..
[34] Q. Li, et al., Photoacoustic spectrum analysis for microstructure characterization using ultra-broad bandwidth optical ultrasonic detector, 2016, vol. 9708, pp. 970812–970812–5.
[35] G. Xu, et al., Photoacoustic and ultrasound dual-modality imaging of human peripheral joints, J. Biomed. Opt. 18 (1) (2013) 010502–010502.
[36] R.K. Saha, M.C. Kolios, A simulation study on photoacoustic signals from red blood cells, J. Acoust. Soc. Am. 129 (5) (2011) 2935–2943.
[37] J. Zalev, M.C. Kolios, Detecting abnormal vasculature from photoacoustic signals using wavelet-packet features, Proc. SPIE vol. 7899 (2011) 78992M–78992M–15.
[38] R.K. Saha, S. Karmakar, E. Hysi, M. Roy, M.C. Kolios, Validity of a theoretical model to examine blood oxygenation dependent optoacoustics, J. Biomed. Opt. 17 (5) (2012) 550021–5500210.
[39] R.K. Saha, A simulation study on the quantitative assessment of tissue microstructure with photoacoustics, IEEE Trans. Ultrason. Ferroelectr. Freq. Control 62 (May (5)) (2015) 881–895.
[40] S. Wang, C. Tao, Y. Yang, X. Wang, X. Liu, Theoretical and experimental study of spectral characteristics of the photoacoustic signal from stochastically distributed particles, IEEE Trans. Ultrason. Ferroelectr. Freq. Control 62 (7) (2015) 1245–1255.
[41] G. Xu, J.B. Fowlkes, C. Tao, X. Liu, X. Wang, Photoacoustic spectrum analysis for microstructure characterization in biological tissue: analytical model, Ultrasound Med. Biol. 41 (5) (2015) 1473–1480.
[42] M.N. Fadhel, E. Hysi, J. Zalev, M.C. Kolios, Photoacoustic simulation of microvessel bleeding: spectral analysis and its implication for monitoring vascular-targeted treatments, Proc. SPIE vol. 9708 (2016) 97081B–97081B–10.
[43] J.P. May, E. Hysi, L.A. Wirtzfeld, E. Undzys, S.-D. Li, M.C. Kolios, Photoacoustic imaging of cancer treatment response: early detection of therapeutic effect from thermosensitive liposomes, PLoS One 11 (October (10)) (2016) e0165345.
[44] S. Mallidi, K. Watanabe, D. Timerman, D. Schoenfeld, T. Hasan, Prediction of tumor recurrence and therapy monitoring using ultrasound-guided photoacoustic imaging, Theranostics 5 (3) (2015) 289–301.
[45] P. Shao, D.W. Chapman, R.B. Moore, R.J. Zemp, Monitoring photodynamic therapy with photoacoustic microscopy, J. Biomed. Opt. 20 (October (10)) (2015) 106012.

[46] T. Tagami, M.J. Ernsting, S.-D. Li, Optimization of a novel and improved thermosensitive liposome formulated with DPPC and a Brij surfactant using a robust in vitro system, J. Controlled Release 154 (September (3)) (2011) 290–297.
[47] T. Tagami, et al., MRI monitoring of intratumoral drug delivery and prediction of the therapeutic effect with a multifunctional thermosensitive liposome, Biomaterials 32 (27) (2011) 6570–6578.
[48] T. Tagami, M.J. Ernsting, S.-D. Li, Efficient tumor regression by a single and low dose treatment with a novel and enhanced formulation of thermosensitive liposomal doxorubicin, J. Controlled Release 152 (June (2)) (2011) 303–309.
[49] J.P. May, S.-D. Li, Hyperthermia-induced drug targeting, Expert Opin. Drug Deliv. 10 (April (4)) (2013) 511–527.
[50] D. Needham, G. Anyarambhatla, G. Kong, M.W. Dewhirst, A new temperature-sensitive liposome for use with mild hyperthermia: characterization and testing in a human tumor xenograft model, Cancer Res. 60 (5) (2000) 1197–1201.
[51] D. Needham, M.W. Dewhirst, The development and testing of a new temperature-sensitive drug delivery system for the treatment of solid tumors, Adv. Drug Deliv. Rev. 53 (3) (2001) 285–305.
[52] A. Needles, et al., Development and initial application of a fully integrated photoacoustic micro-ultrasound system, IEEE Trans. Ultrason. Ferroelectr. Freq. Control 60 (May (5)) (2013) 888–897.
[53] K. Nam, et al., Cross-imaging system comparison of backscatter coefficient estimates from a tissue-mimicking material, J. Acoust. Soc. Am. 132 (September (3)) (2012) 1319–1324.
[54] L.A. Wirtzfeld, et al., Cross-imaging platform comparison of ultrasonic backscatter coefficient measurements of live rat tumors, J. Ultrasound Med. Off. J. Am. Inst. Ultrasound Med. 29 (July (7)) (2010) 1117–1123.
[55] E. Madsen, G. Frank, M. McCormick, M. Deaner, T. Stiles, Anechoic sphere phantoms for estimating 3-D resolution of very-high-frequency ultrasound scanners, IEEE Trans. Ultrason. Ferroelectr. Freq. Control 57 (October (10)) (2010) 2284–2292.
[56] E.L. Madsen, M.E. Deaner, J. Mehi, Properties of phantom tissuelike polymethylpentene in the frequency range 20–70 MHZ, Ultrasound Med. Biol. 37 (8) (2011) 1327–1339.
[57] E. Hysi, D. Dopsa, M.C. Kolios, Photoacoustic tissue characterization using envelope statistics and ultrasonic spectral parameters, Proc SPIE 8943 (2014) 89432E–89432E–9.
[58] L. Wang, K. Maslov, W. Xing, A. Garcia-Uribe, L.V. Wang, Video-rate functional photoacoustic microscopy at depths, J. Biomed. Opt. 17 (10) (2012) 1060071–1060075.
[59] B. Cox, J.G. Laufer, S.R. Arridge, P.C. Beard, Quantitative spectroscopic photoacoustic imaging: a review, J. Biomed. Opt. 17 (June (6)) (2012) p. 61202.
[60] X. Wang, X. Xie, G. Ku, L.V. Wang, G. Stoica, Noninvasive imaging of hemoglobin concentration and oxygenation in the rat brain using high-resolution photoacoustic tomography, J. Biomed. Opt. 11 (2) (2006) P. 24015.
[61] F.L. Lizzi, M. Greenebaum, E.J. Feleppa, M. Elbaum, D.J. Coleman, Theoretical framework for spectrum analysis in ultrasonic tissue characterization, J. Acoust. Soc. Am. 73 (4) (1983) 1366–1373.
[62] F.L. Lizzi, M. Ostromogilsky, E.J. Feleppa, M.C. Rorke, M.M. Yaremko, Relationship of ultrasonic spectral parameters to features of tissue microstructure, IEEE Trans. Ultrason. Ferroelectr. Freq. Control 34 (May (3)) (1987) 319–329.
[63] E.A. Eisenhauer, et al., New response evaluation criteria in solid tumours: revised RECIST guideline (version 1.1), Eur. J. Cancer Oxf. Engl. 1990 45 (2) (2009) 228–247.
[64] R.K. Jain, Molecular regulation of vessel maturation, Nat. Med. 9 (6) (2003) 685–693.
[65] Q. Chen, A. Krol, A. Wright, D. Needham, M.W. Dewhirst, F. Yuan, Tumor microvascular permeability is a key determinant for antivascular effects of doxorubicin encapsulated in a temperature sensitive liposome, Int. J. Hyperthermia 24 (January (6)) (2008) 475–482.
[66] G. Xu, I.A. Dar, C. Tao, X. Liu, C.X. Deng, X. Wang, Photoacoustic spectrum analysis for microstructure characterization in biological tissue: a feasibility study, Appl. Phys. Lett. 101 (November (22)) (2012) 221102.
[67] L.J. Rich, M. Seshadri, Photoacoustic monitoring of tumor and normal tissue response to radiation, Sci. Rep. 6 (February) (2016) P. 21237.
[68] M. Gerling, et al., Real-time assessment of tissue hypoxia in vivo with combined photoacoustics and high-frequency ultrasound, Theranostics 4 (6) (2014) 604–613.
[69] A.A. Manzoor, et al., Overcoming limitations in nanoparticle drug delivery: triggered, intravascular release to improve drug penetration into tumors, Cancer Res. 72 (November (21)) (2012) 5566–5575.
[70] L. Li, et al., Mild hyperthermia triggered doxorubicin release from optimized stealth thermosensitive liposomes improves intratumoral drug delivery and efficacy, J. Control. Release Off. J. Control. Release Soc. 168 (June (2)) (2013) 142–150.
[71] Q. Chen, S. Tong, M.W. Dewhirst, F. Yuan, Targeting tumor microvessels using doxorubicin encapsulated in a novel thermosensitive liposome, Mol. Cancer Ther. 3 (10) (2004) 1311–1317.
[72] G. Xu, et al., High resolution physio-chemical tissue analysis: towards non-invasive In vivo biopsy, Sci. Rep. 6 (February) (2016) P. 16937.
[74] T.N. Erpelding, et al., Sentinel lymph nodes in the rat: noninvasive photoacoustic and US imaging with a clinical US system 1, Radiology 256 (1) (2010) 102–110.
[75] G.J. Czarnota, et al., Ultrasound imaging of apoptosis: high-resolution non-invasive monitoring of programmed cell death in vitro, in situ and in vivo, Br. J. Cancer 81 (October (3)) (1999) 520–527.
[76] M.C. Kolios, G.J. Czarnota, M. Lee, J.W. Hunt, M.D. Sherar, Ultrasonic spectral parameter characterization of apoptosis, Ultrasound Med. Biol. 28 (5) (2002) 589–597.
[77] R.M. Vlad, N.M. Alajez, A. Giles, M.C. Kolios, G.J. Czarnota, Quantitative ultrasound characterization of cancer radiotherapy effects in vitro, Int. J. Radiat. Oncol. Biol. Phys. 72 (4) (2008) 1236–1243.
[78] M.L. Oelze, W.D. O'Brien, J.P. Blue, J.F. Zachary, Differentiation and characterization of rat mammary fibroadenomas and 4T1 mouse carcinomas using quantitative ultrasound imaging, IEEE Trans. Med. Imaging 23 (June (6)) (2004) 764–771.

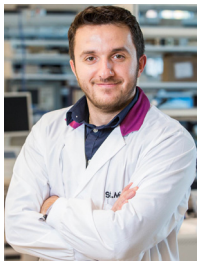

Eno Hysi is a PhD candidate in the Department of Physics at Ryerson University and a Vanier Scholar. Eno received his BSc degree in 2010 from Ryerson University (Toronto) in Medical Physics where he was first introduced to photoacoustic imaging. He continued his research at Ryerson's Department of Physics where, in 2012, he graduated from his MSc in Biomedical Physics with a Gold Medal. His MSc research resulted in a number of publications and he co-authored a book chapter. Throughout his studies, Eno has been the recipient of numerous academic awards and scholarships including the Ontario Graduate Scholarship, NSERC's Alexander Graham Bell Canada Graduate Scholarship and most recently the Vanier Canada Graduate Scholarship. His research interests include ultrasound and photoacoustic tissue characterization.

Lauren A. Wirtzfeld was born in Toronto, Ontario. She earned her B.A.Sc. degree in engineering science, biomedical engineering option, in 2003 from the University of Toronto, Toronto, Canada, and her Ph.D. degree in biomedical engineering from the University of Western Ontario in 2008. Dr. Wirtzfeld was a postdoctoral fellow at the University of Illinois at Urbana-Champaign from 2009 to 2011. Currently, Dr. Wirtzfeld is a postdoctoral fellow at Ryerson University, Toronto, Canada, where she is conducting research in medical ultrasound. Her research interests include quantitative ultrasound, tissue characterization, and applications of ultrasound and photoacoustics for monitoring cancer treatment response.

Jonathan P. May is a chemist that has turned his hand to the area of Drug Delivery, particularly for the treatment of cancer. He received his PhD in Biological Chemistry from the University of Southampton, UK. Jon received a travelling fellowship from the Royal Society to take a post-doctoral fellow position in the Chemistry department of UBC working on synthesis of the bicyclic peptide natural products, the amatoxins. Following this he took a position at the Centre for Drug Research and Development, Vancouver working in Medicinal Chemistry, and later on at the Ontario Institute for Cancer Research, Toronto where he worked in the Drug Delivery and Formulation group as part of the Drug Discovery Platform. Jon developed a Thermosensitive Liposome (TSL) platform called HaT (Heat activated cytoToxic), which could deliver multiple drugs and utilize citrate or copper active loading methods. Most recently he has been studying the TSL formulation and its effects on the tumor in the search for a reliable marker for treatment efficacy within a few hours post-treatment. Since moving back to UBC with Prof. Li, Jon has taken on a more active role in the teaching and supervision of students in the Chemistry and Drug Delivery area.

Elijus Undzys is research associate with veterinary medicine background working at the Ontario Institute for Cancer Research, Drug Discovery Platform in Toronto, Canada. He has diverse experience in preclinical studies in oncology and central nervous system disorders field. Elijus' research focuses on using and advancing drug delivery techniques and technologies in various different applications.

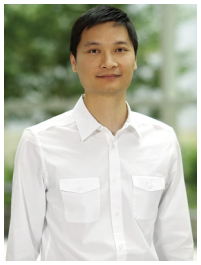

Shyh-Dar Li is an Associate Professor at the Faculty of Pharmaceutical Sciences, University of British Columbia. He holds the Angiotech Professorship of Drug Delivery. His research focuses on developing innovative drug delivery technologies to enhance cancer therapy with a particular interest in lipid and polymer based nanoparticles. His research program has been supported by federal funding including National Institutes of Health (NIH) and Canadian Institutes of Health Research (CIHR).

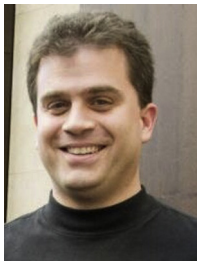

Michael C. Kolios is a Professor in the Department of Physics at Ryerson University and associate Dean of Research and Graduate Studies in the Faculty of Science. His work focuses on the use of ultrasound and optics in the biomedical sciences. He has published 73 peer-reviewed journal publications, 5 book chapters, and 96 papers in conference proceedings. He has been invited to speak at 35 different organizations or conferences, and has been the keynote and plenary speaker for conferences in Canada, India and China. He has received numerous teaching and research awards, including the Canada Research Chair in Biomedical Applications of Ultrasound and the Ontario Premier's Research Excellence Award. He is on the editorial board of the journals Ultrasound Imaging and Photoacoustics and is member of many national and international committees, including the IEEE International Ultrasonics Symposium Technical Program Committee. He is a member of the National Institutes of Health (NIH) Biomedical Imaging Technology A study section and was previously a member of the Canadian Institutes of Health Research (CIHR) Medical Physics and Imaging (MPI) panel.